LANGMUIR

Design of a Humidity Sensor for a PPE Kit Using a Flexible Paper Substrate

Priyanka Chaudhary, Arpit Verma, Sandeep Chaudhary, Mahesh Kumar, Meng-Fang Lin,* Yu-Ching Huang,* Kuen-Lin Chen, and B.C. Yadav*

Read Online

ACCESS | Metrics & More | Article Recommendations | Supporting Information

ABSTRACT: The present work reports the rapid sweat detection inside a PPE kit using a flexible humidity sensor based on hydrothermally synthesized ZnO (zinc oxide) nanoflowers (ZNFs). Physical characterization of ZNFs was done using scanning electron microscopy (SEM), X-ray diffraction (XRD), Fourier transmission infrared spectroscopy (FTIR), UV−visible, particle size analysis, Raman analysis, and X-ray photoelectron spectroscopy (XPS) analysis, and the hydrophilicity was investigated by using contact angle measurement. Fabrication of a flexible sensor was done by deposition on the paper substrate using the spin coating technique. It exhibited high sensitivity and low response and recovery times in the humidity range 10−95%RH. The sensor demonstrated the highest sensitivity of 296.70 nF/%RH within the humidity range 55−95%RH, and the rapid response and recovery times were also calculated and found as 5.10/1.70 s, respectively. The

selectivity of the proposed sensor was also analyzed, and it is highly sensitive to humidity. The humidity sensing characteristics were theoretically witnessed in terms of the highest occupied molecular orbital (HOMO) and lowest unoccupied molecular orbital (LUMO) and electronic properties of sensing materials in ambient and humid conditions. These theoretical results are evidence of the interaction of ZnO with humidity. Overall, the present study provides a scope of architecture-enabled paper-based humidity sensors for the detection of sweat levels inside PPE kits for health workers.
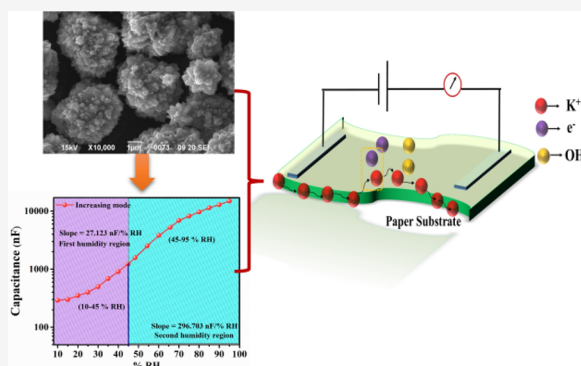
INTRODUCTION

Presently, both young and elderly individuals are increasingly focusing on their healthcare status. Consequently, there is a growing interest in medical monitoring devices that offer high performance, comfort, compact size, high flexibility, and the ability to detect physiological information such as sweat levels through point-to-electronic devices.[1] The coronavirus disease 2019 (COVID-19) pandemic has increased rapidly all over the world, so this is a measured challenge for regular health care. Healthcare workers have continuously protected us using a personal protective equipment (PPE) kit, which provides absolute shield protection for fighting disease spread in the world. However, wearing these PPE kits has various problems, including dehydration, sweating, etc.[2] There is an urgent need to consider these problems faced by healthcare workers (HCWs) both qualitatively and quantitatively. An electronic wearable device can be used in a PPE Kit that detects the moisture level[3] or sweat level and gives a signal in the form of an alarm. According to the electronic survey of HCWs who had performed COVID-19 duties while wearing the PPE kits, they expressed many problems.[4] The most common problems while using the PPE kits were extreme sweating (100%), clouding on the surface of goggles (88%), suffocation (83%),

breathlessness problem (61%), tiredness (75%), headache due to continuous use of this kit (28%), and pressure marks on the skin on more areas on repetitive use (19%).[5]

Sweating in the human body is a form of thermoregulation where 500 and 700 mL of hypotonic fluid is stowed by the sweat glands of the human body under environmental conditions. Sweat is easily excreted from the skin surface of the human body and contains sodium ions, potassium ions, and metabolites such as glucose.[6] Generally, human sweat mainly contains 99% water with a negligible proportion of salt and fat.[7] In this context, precise monitoring of sweating levels inside PPE kits is highly urged as an effective preventive measure against COVID contamination. In this work, we have proposed a moisture detector for sweat with an alarm system device that will give a signal during high sweat levels inside the PPE kit.[8] For humidity sensing, researchers have been focused
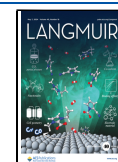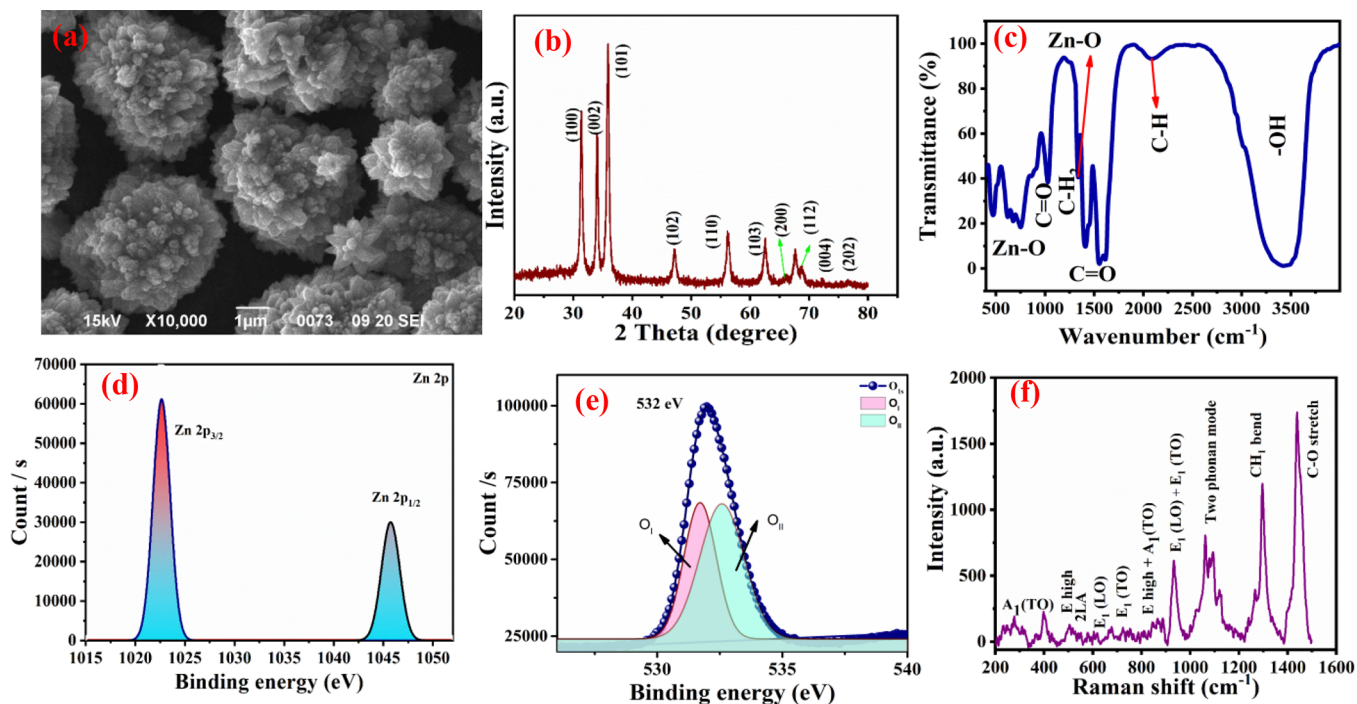
Figure 1. Morphological and structural analysis of ZNFs: (a) surface morphology, (b) XRD diffraction pattern, (c) FTIR analysis, XPS analysis of the (d) zinc element and (e) oxygen element, and (f) Raman analysis.

on a variety of materials, such as metal oxides, ceramics, carbon compounds, perovskites, polymers, etc.[9]

In particular, metal oxides such as ZnO,[10] CuO,[11] Al_2O_3, and others[12] are widely used for sensor development due to their simple fabrication, high sensing response, good operational stability, low cost, and good portability. Chen and Zhang investigated ZnO nanostructure, synthesized by thermal decomposition and controlled via dielectrophoresis, application as a capacitive relative humidity sensor, and the response and recovery times have been reported as 20 and 70 s, respectively.[13] Yu et al.[14] explored ZnO becoming widely studied as a humidity-sensing material because it is abundant and has controllable surface morphology, wide resistivity range, and good chemical stability. The currently reported ZnO metal oxide has poor electron mobility, a small specific surface area, and no hydrophilic functional groups on its surface, which significantly restricts its development as a humidity sensor.[10] The ZnO-based humidity sensor may be improved with a variety of materials, including composites and doping.[15,16] Enhancing the sensing parameters, including the response and recovery times, has emerged as a prominent research area in the field of metal oxide-based sensors.[17] Zinc oxide is a nontoxic and high-adsorption material due to more oxygen vacancies attached to its structure.[18,19]

A low-cost, biocompatible, flexible, and wearable sweat-sensing device based on ZNFs was proposed in the present work. We have systematically investigated its humidity sensing properties, such as sensitivity, aging, stability, and flexibility. Several reasons were proposed for the important increased sensitivity of using the ZNFs. First, the adhesion of the material on the substrate may increase the sensitivity of the material. This flower-like surface provides more active sites during the adsorption and desorption of water molecules. Second, the surface functional group and hydrophilic nature of the sensing material can be responsible for enhancing the

adsorption of water molecules. A statistical survey has also been conducted involving healthcare workers of different ages showing the problem of wearing the PPE kit for a long time. The present work also includes a theoretical study that investigates the HOMO−LUMO gap, electronic properties, and interaction between ZnO and water molecules. This analysis sheds light on the impact of humidity on the structure of the ZNFs. All of these parameters, as observed during both experimental and theoretical studies, demonstrate significant promise for the detection of humidity levels within the PPE kit.

■ EXPERIMENTAL SECTION

Materials and Methods. Zinc nitrate hexahydrate $[Zn(NO_3)_2 \cdot 6H_2O]$ (99%, Thermo Scientific Chemicals) and sodium hydroxide $[NaOH]$ (99.9%, pellets from Thermo Fisher) were purchased. All chemicals were used in analytical grade without further purification.

Synthesis via the Hydrothermal Method. The ZNFs were synthesized by a hydrothermal route; for this purpose, 0.3 M Zn $(NO_3)_2 \cdot 6H_2O$ solution was dissolved in 20 mL of an aqueous solution under constant stirring for 50 min. Meanwhile, 4 M NaOH was also prepared in 20 mL of aqueous solution under constant stirring for 30 min. After that, the NaOH solution was dropwise added to the previous solution. The mixture of this solution was transferred into sealed Teflon-lined stainless-steel autoclaves and put in an oven for hydrothermal treatment at 150 °C temperature for 2 h.[20] Then the autoclave was taken outside from the oven and allowed to cool at ambient temperature. The solution was filtered with filter paper and centrifuged several times. The precipitate was found and dried for 2 h in the oven. This method is different from other reported methods because no capping agent was used during the synthesis; owing to this reason, it is suitable for processing, is nontoxic, and is low cost. The block diagram and possible reaction are shown in FigureS1a.

Fabrication of the Sensing Element and Sensing Setup. The fabrication of the sensing device has been already reported by our group and is shown in Figure S1b.[21] Initially, a small amount of ZnO powder was dissolved in NMP solvent, and this was ultrasonicated for clear dispersion. Further, cellulose paper was cut into the desired shape and size. Then this paper substrate was fixed (one by one) on

the spin coater of the ZnO dispersant on paper substrate at 1000 rpm. This process was repeated three times to obtain uniformity of the device. Again, these devices were dried under ambient atmospheric conditions, and silver paste was painted for the electrical measurement.

The sensing setup consisted of many constituents such as an impedance analyzer (Wayne Kerr Precision Component Analyzer, 6440B), a Keithley 6517B, and a sensor made of ZNFs that was tested for its ability to detect humidity inside the chamber and sweat level inside the PPE kit. To maintain the humidity levels inside the glass chamber, saturated salts of K_2SO_4 and KOH solutions were used and retained by the static process. The flexible sensing element's %RH concentration was used using a K_2SO_4 solution to increase it and KOH to reduce it. Using a hygrometer (HTC-1), the relative humidity (%RH) was precisely measured. Interdigitated electrodes made of silver paste were imprinted with wires connecting them to an impedance analyzer on the sensing screen. The entire experiment was conducted at 300 K above ambient temperature. The sensing setup is also depicted in Figure S2.[22]

■ RESULTS AND DISCUSSION

Figure 1a shows the SEM images of the ZNFs exhibiting a uniform flower morphology with diameters of approximately 72.62 nm. Furthermore, these images with different magnifications show the flower made with the combination of the rods as displayed in Figure S3a,b. To achieve the desired hierarchical, flower-like structure, ZnO nanoflowers need thorough control over reaction conditions, surfactant selection, and ongoing refining. The unique crystal growth mechanism during the synthesis procedure can give rise to nanoflower formations. ZnO nanoparticle generation is a result of nucleation followed by crystal growth. Morphologies, such as nanoflowers, can arise from the circumstances surrounding nucleation and development. The facets of the ZnO crystal structure may have controlled the crystal growth, producing an arrangement that looks like a flower. The formed flower plays an important role in the sensing element because of the high surface-to-volume ratio, which provides high adsorption and desorption capacity. The X-ray diffractometer (PANalytical, Netherlands) with Cu Kα radiation (λ = 0.15406 nm) used to study the structural analysis of ZNFs is shown in Figure 1b. The Miller indices (100), (002), and (101) correspond to the peaks at angles of 31.85, 34.51, and 36.33°, respectively. The Debye−Scherrer formula[23] is used to calculate the average crystallite size, which is found to be 30.18 nm, where k is the Scherrer constant. The signature peaks positioned at 45.80, 52.59, and 62.47° correspond to Miller planes (100), (200), and (103) of ZNFs respectively.[24] The presence of ZNFs is shown in planes (112), (004), and (202) in Figure 1b. From the XRD analysis, we can conclude that there is no impurity of the synthesized material. One other characterization for the confirmation of the pure ZNFs is the FTIR (Fourier transform infrared) spectrum, as shown in Figure 1c, which is connected to the vibrational modes of the Zn−O bonds in the crystal lattice. These peaks can reveal details of the chemical and structural peaks of ZnO as well as any impurities that might be present. The given peaks correspond to the infrared spectra of ZNFs. The peak at 3432.67 cm^{-1} relates to the stretching vibration of the hydroxyl (OH) groups that may be present on the surface of ZNFs, and the peak at 2076.95 cm^{-1} corresponds to the stretching vibration of C−H bonds. Because of this peak, the ZNFs exhibit hydrophilicity, and it is responsible for good humidity adsorption and desorption.

The peak at 1556.12 cm^{-1} can be assigned as the bending vibration peak at 1398.13 cm^{-1} that corresponds to the

symmetric stretching vibration of H−O−H, whereas the peak at 1340.54 cm^{-1} corresponds to the asymmetric stretching vibration of Zn−O−Zn bonds in ZNFs.[25] The peak at 1031.73 cm^{-1} corresponds to the bending vibration of the Zn−OH bonds, which could be due to the presence of water or hydroxyl groups on the surface of ZnO shown in Figure 1c. The peak positioned at 611.32 cm^{-1} , and 464.76 cm^{-1} corresponds to the bending vibration of Zn−OH bonds,[26,27] which could be due to the presence of water or hydroxyl groups on the surface of ZNFs. . FTIR analysis provides the purity of ZNFs and the hydrophilic functional groups that will be responsible for the sensing application. The elemental analysis confirmed by the convoluted electrical structure of solids can be studied using X-ray photoelectron spectroscopy.[28] Regarding the excitation source, we used a standard Al Kα X-ray source. The electron emission angle was kept at a fixed 45° angle with respect to the sample surface. The size of the analyzed area was approximately 1 mm in diameter. Prior to the analyses, the samples were sputter-etched using an Ar^+ ion beam with energy of 2 keV and an incidence angle of 60°. The base pressure during the analyses was approximately 10^{-9} Torr, and a charge neutralizer was used to minimize the effect of charging on the spectra. The C 1s element was used for charge adjustment. To adjust the binding energies of other elements in the spectrum, the standard element's binding energy was utilized as a guide. Shirley background mathematical functions were used to simulate the background in XPS peak fitting. The Lorentzian function was used to simulate the XPS peaks in the Origin software.[29] The peak profiles around the Zn $2p_{3/2}$ and Zn $2p_{1/2}$ peaks were similarly fitted, with the peak energies being 1022.25 and 1045.31 eV, respectively. These emissions are related to Zn atoms located in ZnO's normal lattice location. It was observed that the binding energies' difference between the Zn $2p_{3/2}$ and Zn $2p_{1/2}$ emissions in this instance was 23.06 eV, which is the typical value for ZnO. The Zn LMM Auger peak analysis is frequently utilized to determine the chemical states of the Zn species because it has been previously observed[30] that the Zn $2p_{3/2}$ peak shape does not always exhibit an asymmetric feature shown in Figure 1d. Because a single Auger transition involves three electrons and several physical effects, Auger peaks typically exhibit bigger shape variations than XPS peaks with different chemical states.[31]

From Figure 1e, the existence of oxygen interstitials (Oi) and oxygen vacancy (VO) point defects in ZnO can be identified in this context by XPS analysis. It was previously observed that the O_{1s} state always has three binding energy components, which correspond to at 532.40 eV. And this peak is attributed to oxygen or hydroxyl (OH) species that have chemisorbed or dissociated on the surface of the ZNFs.[32] In a different study, two unique Gaussian curves with centers at 530.28, 531.30, and 532.36 eV, , were attributed to oxygen atoms at regular lattice sites (OL), oxygen-deficient locations (e.g., VO), interstitial O (Oi), or surface oxygen atoms, respectively and the peaks are confirmed by the previous literature.[32] A greater BE shift is caused by O_i, which stands for more oxygen atoms inside the crystal lattice, whereas a lower BE shift is caused by V_O, which is for missing oxygen atoms. Because of their disruptive effect on the crystal lattice, point defects are characterized by peak widening and changes in peak shape.[33,34] Peak fitting is done with the Origin-09 software to break down the O 1s peak into many components, which aids in differentiating between the various chemical states of

oxygen, such as O_i and V_O. These results showed the confirmation of the pure Zn−O bonds with the presence of electronic states.[35] The electrical conductivity, high surface-to-volume ratio, and surface oxygen vacancies have played an important role as a sensor due to oxygen vacancies that are responsible for the adsorption and desorption of the humidity. The sensitivity also increased as a result of oxygen molecules because they interact with H_2O and make the hydronium that increases the conductivity of the sensing film.

Raman spectra also give information about the Raman active modes of the ZNFs often exhibiting a variety of peaks that are connected to the vibrational modes of the Zn−O bonds and the crystal lattice structure. Determining the characteristics of ZnO, such as the strain, flaws, and crystal quality, is possible with the aid of Raman spectroscopy. The 278.03 cm^{-1} peak corresponds to the LO (longitudinal optical) phonon mode, which involves the vibration of the Zn and O atoms in the crystal in a direction perpendicular to the c axis. From Figure 1f, the peak at 397.89 cm^{-1} corresponds to the E_2 high phonon mode, which involves the vibration of the Zn atoms in the lattice, and the peak at 504.13 cm^{-1} corresponds to the $E_1(TO)$ phonon mode, which involves the vibration of the oxygen atoms in the lattice. Another peak at 932.89 cm^{-1} corresponds to a combination of the $E_1(TO)$ and $E_2(high)$ modes.[32] The 1063.02 cm^{-1} peak can be assigned to the $A_1(TO)$ phonon mode, which involves the vibration of oxygen atoms in the lattice. The peak at 1295.87 cm^{-1} can be recognized as the $E_1(LO)$ phonon mode, which involves the vibration of the oxygen atoms in the lattice in a direction parallel to the c axis, and the 1438.20 cm^{-1} peak can be recognized as the second-order LO (LO-2) phonon mode, which involves the formation of two LO phonons. The Raman spectra helped to confirm the chemical forms, and this is very important for the purity of the material.

The graph of $(\alpha h\upsilon)^2$ versus photon energy ($h\upsilon$), where is the α is absorption coefficient and h is the photon energy, the value of bandgap was calculated by this formula. The optical band gap energy of a semiconductor material, such as ZNFs, is frequently determined and shown in Figure S3c. Typically, UV−visible spectrophotometer or other optical methods are used to determine the absorption coefficient in a Tauc plot of ZNFs as a function of photon energy.[36] Hence, the band gap energy may be roughly determined by the Tauc plot approach and was found to be 3.70 eV. This band gap is close to the electronic band gap of the ZNF material; the obtained results show that the produced ZNFs possessed wide optical band gaps, good crystallinity, and good monodispersity in the nanosize range. The optical band gap of the ZNF film was calculated before and after exposure to humidity. From the results, we can observe that the band gap increased from 3.7 to 3.9 eV. At the same time, a decrease in ZnO conductivity is shown by the band gap values increasing. The resistance of the metal oxide increased with the increase in the band gap. The wide gap reduced the concentration of charge carriers in their conduction. In the context of ZnO, the increase in energy band gap upon humidity exposure is anticipated to alter the electronic structure of ZnO. The successive change in humidity concentration led to the introduction of defects in ZnO. These defects act as a trapping center within the materials' band gap for humidity absorption that causes the change in the optical characteristics of metal oxide. Consequently, there is an increase in the required energy values observed for electrons to transition from the valence band to the conduction band. This

behavior is widely found in metal oxide semiconductors such as zinc oxide (ZnO) and titanium dioxide (TiO$_2$) for a variety of reasons, including the ability of water molecules to dissociate into hydroxyl groups (OH−) and protons (H+) when they adsorb onto the surface of these materials. The presence of these hydroxyl groups can alter the electrical structure of the metal oxide surface.[37] Dynamic light scattering (DLS) was used to precisely analyze the average particle size of ZNFs, as shown in Figure S3d. DLS analysis reveals the Brownian motion of the scattered particles, and the average particle size of the particles is calculated. The ZNF's average particle size distribution ranges from 40 to 120 nm. These results were also verified with SEM and XRD analysis. The SEM images presented the zinc oxide grown as the flower -like structure with the combination of rods or leaf. The size of the leaf confirmed by the XRD analysis and its also showing the high surface area. From the results its confirmed ZNF is the promising material for humidity sensing, which is responsible for the adsorbed the desorbed water molecules easily.

Sensing Mechanism. The water vapor is known to be adsorbed on the surface of ZNFs and reacts reversibly with the ZnO lattice. The possible reaction is shown in eq 1:

$$H_2O + O^+ + 2Zn \leftrightarrow 2(OH-Zn) + V_O\bullet\bullet + 2e-$$

$$(1)$$
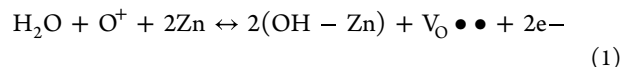
where O represents the oxygen atom at the oxygen site and $V_O\bullet\bullet$ represents the vacancy formed at the oxygen site. Ionic Zn^{2+} will induce chemisorption followed by physisorption of water molecules in the increasing number of free electrons at a high RH medium, and NFs should become more conductive.[38] Initially, the film was free of water molecules; therefore, no interaction between water and zinc oxide is shown in Figure 2a. In the region with mid humidity (10−45% RH), the
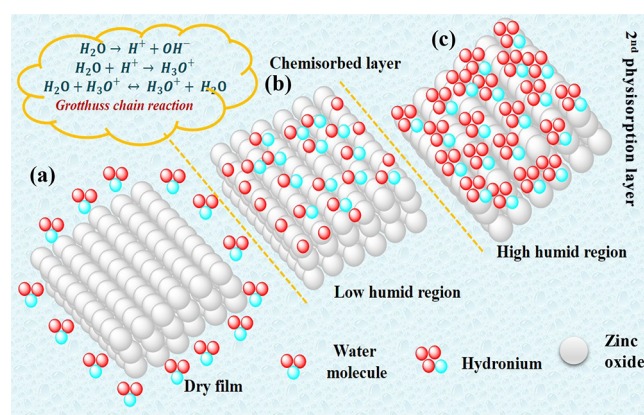

Figure 2. Humidity sensing mechanism. (a) ZNFs free from water molecules, (b) low-humidity region, and (c) high-humidity region.

adsorption rate of water molecules increases, and a chain of water molecules is formed on the zinc oxide sensor film by a chemisorption process shown in Figure 2b. In this range, the capacitance increases rapidly, and simultaneously, resistance decreases because of this proton transport, which increases the conductivity of the sensing element, with the increase of the sensitivity as ~27.13 nF/%RH. At the high-humidity region (45−95% RH), the formation physisorption of the layer was triggered by the proton ions jumping through the chemisorption layer as can be observed in Figure 2c. When they interact with the water molecules, they form hydronium ions,
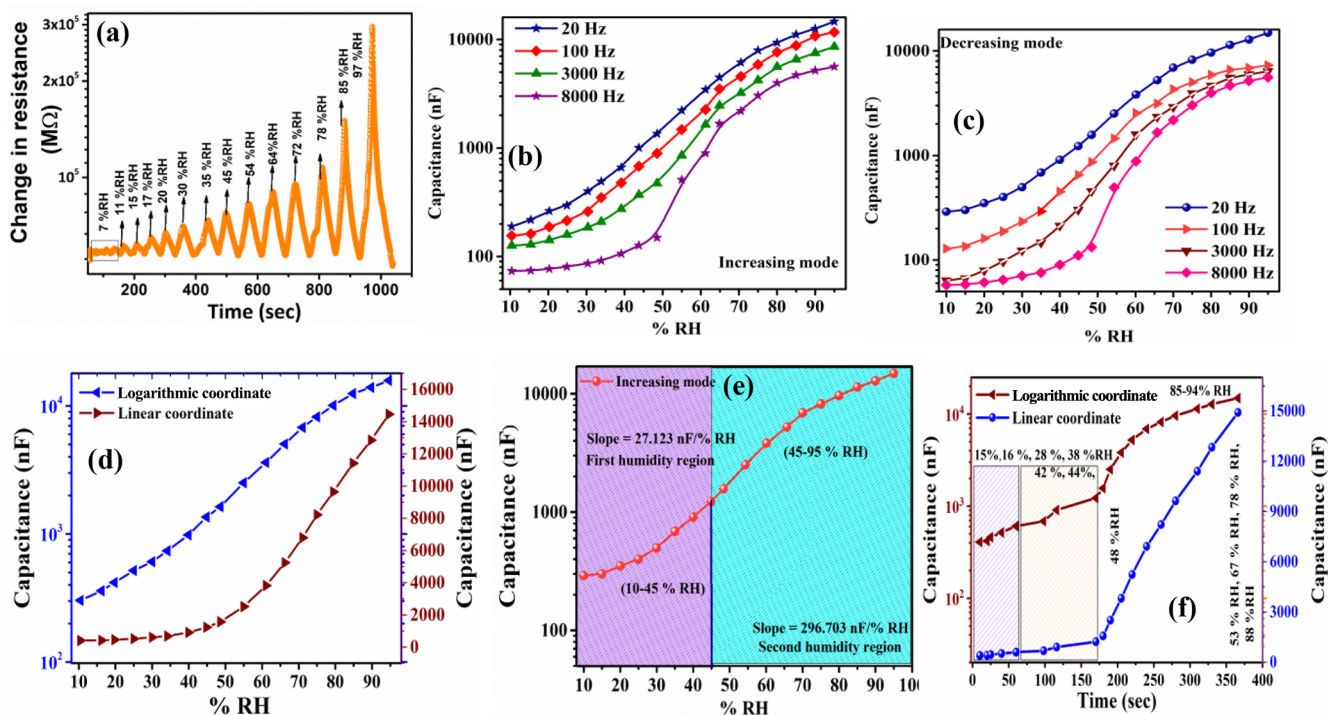
Figure 3. Variation of electrical parameters at a different relative humidity. (a) Change in resistance with respect to time; (b, c) capacitance absorption and desorption of humidity at 20, 100, 3000, and 8000 Hz; (d) capacitance at logarithmic scale with respect to relative humidity; (e) sensor performance as sensitivity by linear fitting in both regimes at 20 Hz; and (f) humidity sensor response at logarithmic scale concerning time.

and the capacitance was again increased because of the condensation of the capillary in the pores of the sensing element, and the sensitivity is high at ~296.70 nF/%RH at an optimum frequency of 20 Hz for ZNFs.

Humidity Sensor Measurement. The change in resistance corresponding with time variation at different relative humidity was recorded and is presented in Figure 3a. The plot makes it clear that, over time, as the humidity level rises (10 to 95%RH), the resistance provided by the sensing film also rises. An impedance analyzer was used to analyze capacitance values at each level of humidity. The variation in capacitance corresponding to %RH is also represented as a function of frequency (20, 100, 3000, and 8000 Hz,) presented in Figure 3b. From the curve, it is obvious that the capacitance reduces with rising frequencies but rises with increasing humidity.[39] Low humidity levels are ideal for a capacitive humidity sensor because there is less adsorption of water molecules. The presence of space charge polarization in adsorbed water molecules causes the direction of the electric field to slowly change at low frequencies. To avoid the adsorbed molecules' polarization from interacting with the electric field, the direction of the electric field abruptly reverses at a higher frequency.[40] As a result, the resistance is low and independent of humidity (%RH). According to the sensing curve, the capacitance value changes from 114.21 to 14,614.10 nF, which provides the sensing material's high sensitivity (S ~296.70 nF/%RH) at a greater humidity range. The detailed sensitivity for each humidity regime is presented in Table S1. At 8000 Hz, there was a very minor shift in capacitance from 74.56 to 5611.12 nF when compared to other frequencies, and the sensitivity was determined to be S ~67.44 nF/%RH across the full range of 10−95%RH.

It is clear from Figure 3c in the variation of capacitance with respect to humidity at decreasing mode that when relative humidity increases from 30 to 94%RH, the capacitance rate decreases monotonically in the same manner. Inside the humidity chamber, the relative humidity increases as the ZNF sensor's capacitance value increases. Adsorbed water molecules on the surface enable polarization and increase the dielectric constant of sensing materials, which is the cause of this sensing property.[41] The value of capacitance varies with relative humidity in all frequency domains; however, the major variation in capacitance value is low in the higher-frequency regime. The value of capacitance swings with relative humidity in all frequency regimes, but in the higher-frequency regime, the abrupt shift in capacitance value is small, and humidity management becomes self-governing.[42] The capacitance and humidity detection performance of humidity sensors, especially capacitive ones, are significantly influenced by the test frequency. The test frequency and capacitance have a nonlinear connection that influences how these sensors react to variations in humidity. Lower test frequencies give the sensing element more time to respond to changes in humidity, which cause more noticeable capacitance fluctuations. As a result, the sensor is better suited to recording slow changes in the humidity. Very low frequencies, however, may increase the sensitivity of the sensor to outside noise and drift.[43] Higher test frequencies, on the other hand, might result in smaller capacitance changes and shorter reaction times, which can lessen sensitivity to tiny changes in humidity.[44] While taking the trade-off between sensitivity and reaction time into account, the test frequency selection should be in line with the needs of the application. Lower frequencies above 8000 Hz can detect the transferable humidity level. Instead of the frequency of the applied AC, the relative humidity in the
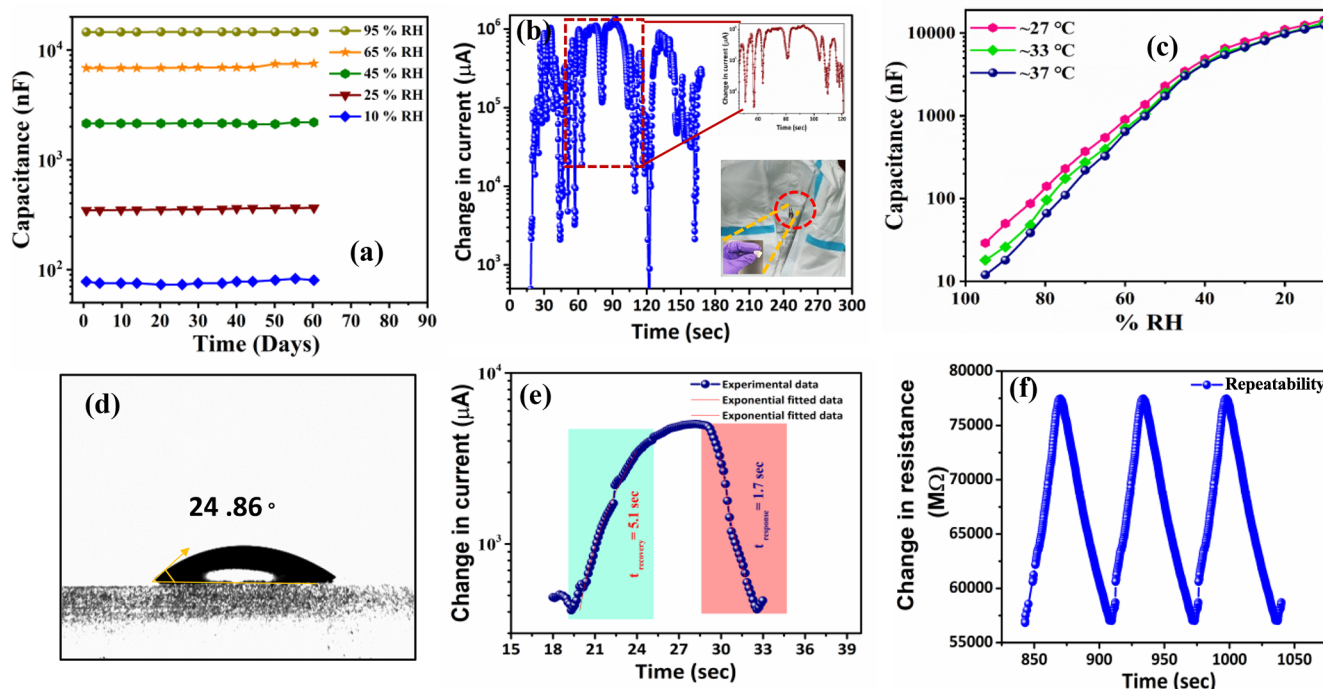
Figure 4. Other parameters of the ZNF humidity sensing device. (a) Stability curve at 20 Hz frequency, (b) sweat measurement sensor response in the PPE kit, (c) sensor response at different body temperatures, (d) contact angle measurement of ZNFs, (e) dynamic sensor response and recovery times of the proposed sensor, and (f) repeatability test at 45%RH.

immediate environment has a greater impact on a sensor's capacitance value. However, it is significant to learn that variations in the AC signal's frequency might still have an impact on how much capacitance is measured. The dielectric characteristics of the sensing material or the space between the sensor plates are affected by the relative humidity in a capacitive humidity sensor. The material's dielectric constant or effective dielectric thickness fluctuates in response to exposure to various humidity levels, causing a shift in capacitance values. Usually, capacitive sensors detect capacitance using an AC signal. A consistent voltage across the sensor's components can be maintained by delivering an AC voltage, assisting in avoiding problems.

As can be seen from the curve in Figure 3d, the optimum linearity for sensing characteristics was discovered in the range of 45 to 95%RH at the lowest frequency of 20 Hz. The linear fitting was used to analyze of sensitivity of the material as shown in Figure 3e. Sensitivity was calculated at both low- and higher-humidity regions, and it was found as S ~296.70 nF/% RH. Figure 3f shows the humidity sensor response on a logarithmic scale over time, with a nonlinear curve ranging from 10 to 95%RH.[45] The stability and responsiveness, hydrophilicity, repeatability, and recovery time with different temperatures are also studied and shown in Figure 4a−f. Figure 4a depicts the stability of the capacitive humidity curve at 20 Hz frequency. For 60 days, we investigated the parameters of flexible humidity sensor elements at 20 Hz under different relative humidity levels of 15, 35, 55, 75, and 95%. The humidity detection occurred every 5 days.

Long hysteresis is a negative parameter for any sensor, including capacitive humidity sensors, because it causes the detecting material to change, lowering sensor performance. The hysteresis characteristic is an important statistic for determining the sensor accuracy. Using the equation presented in the prior literature, hysteresis was computed as 2.5%RH

from. The hysteresis of a ZNF film sensor was studied by exposing it to different humidity levels ranging from 10 to 95% RH followed by desorption from 95 to 10%RH. The hysteresis curve in adsorption and desorption mode at 20 Hz frequency is shown in Figure S4, as calculated by eq 2. As can be shown, our humidity sensor has a low hysteresis characteristic for the sensing material.[46]

$$\text{Hysteresis} = \frac{\text{capacitance}_{\text{desorption}} - \text{capacitance}_{\text{adsorption}}}{\text{sensitivity}}$$

$$(\%\text{RH}) \qquad\qquad (2)$$

Natural changes in the environment, such as temperature variations inside the PPE kit, are the main reasons for the irregularities of the response. The sensor's response is measured in terms of changes in conductivity over time as it interacts with sweat. The corresponding data shown in Figure 4b and the inset data again presented at short scale the confirmation that the sensor responded after the adsorption of sweat. When the data are plotted in a short range, the irregular pattern and also the combination of cycles of sensor response are clearly shown in the inset of Figure 4b. The device was placed inside the PPE KIT, and after 2 h, measurement was taken when the body temperature reached ~32 °C. Because of sweat inside the body, the temperature changed. We carried out the humidity sensing experiment at body temperature (37 °C), and Figure 4c illustrates this. Because body sweat is like a conductor and a conductor does not depend on humidity, relative humidity increases while temperature decreases for a few minutes. And the data have been recorded at three temperatures: 27, 33, and 37 °C.

The hydrophilicity of a sensing material can be determined by measuring the contact angle between water droplets on the sensor surface. The water contact angle measurements showed that the angle is 24.84°, which is less than 90°. From the
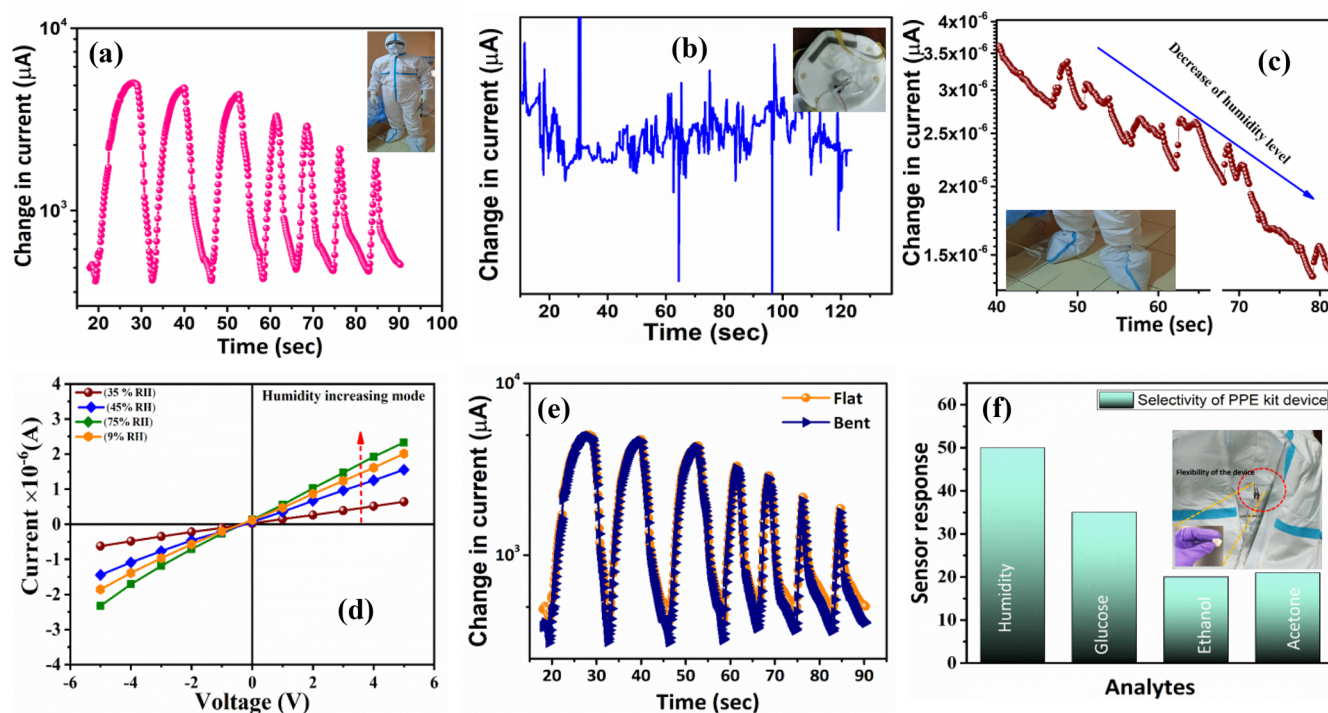
Figure 5. Variation of electrical parameters of the ZNF humidity sensor in the PPE kit. (a) Current with respect to time, (b) detection of moisture level inside the mask, (c) sensor response in PPE kit shoes, (d) current−voltage at different relative humidity, and (e) dynamic sensor response at flat and bent (f) selectivity of the sensor with different analytes.

contact angle, it presented a hydrophilic nature, and the ZNFs showed good wettability as shown in Figure 4d. At this lowest angle, we can say that the sensor is highly hydrophilic in nature and has excellent properties for any humidity sensor. The response and recovery times are very essential characteristics displayed in Figure 4 e, which confirmed the time of sensor response from its environmental condition, and the recovery time reveals that the time sensor reaches the original position. The response and recovery times were calculated to be 5.10 and 1.70 s, respectively. The humidity sensor based on ZNFs demonstrated excellent repeatability at the same condition of the sensor. We examined the sensor at 45%RH as shown in Figure 4f, and the sensor exhibited repeatability. The comparison of other reported humidity sensing devices is also presented in Table S2, which shows that this ZNF paper-based humidity sensor has the best response and recovery times as compared to other reported composite materials with ZnO.

Sweat Level Measurement inside the PPE Kit Sensors. In Figure 5a, the variation of current with respect to time is shown as humidity in and humidity out. This study shows that the material is highly responsible for sweat measurement. The sensor was also tested inside the mask, and it exhibits high responsiveness, as shown in Figure 5b. From Figure 5c, it can be observed that the ZNFs are responsive for the shoes of the PPE kit. This exhibits that the sensor is highly responsive for the entire PPE kit. Figure 5d displays the current variation with voltage at 35, 45, 75, and 95%RH (relative humidity). Figure 5e presents the flat and bent sensors used in a humidity sensing experiment under comparable test conditions. It is clear that the current of the flat and bent sensors was almost identical for the relative humidity range of 10 to 95%RH. At high humidity levels, a little variation in the current versus %RH curve has been seen.

This might be because humidity absorbs at different rates in flat and bending circumstances. The dynamic sensing properties of humidity sensors such as humidity absorption and desorption under flat and bent situations are depicted in Figure 5e. Additionally, the sensor demonstrated a reliable response across several test cycles under both flat and bending circumstances without any degradation. These deformation characteristics show the flexibility of the sensing device. Selectivity is an important criterion for any sensing device, so different analytes were used during the sensing performance. Figure 5f shows the selectivity of the zinc oxide nanoflower. After the water molecule, glucose is the second one that has a high percentage during sweating, so we have tested analytes such as glucose, ethanol, and acetone. The sensing material may affect the accessibility and diffusion of analytes, and specific interactions affect the selectivity and sensitivity of the device for each analyte. An interesting finding from the testing is that the sensing device is highly responsive to humidity for the ZnO nanoflower.

The statistical analysis was also done, and data are presented in Figure S5a. We have taken the data from King George's Medical University Hospital, Lucknow, India. The survey also presented that the sweat level increased, and many more problems were detected such as dizziness, loss of breathing, sweating, and headache. As age increases, the sweat level timing also increases, as presented in Figure S5b.

DFT Analysis. The Gaussian 09 program was used to form the ZnO molecules, and the structures were then optimized with interaction of water molecules and without water molecules.[47] In this optimization procedure, the ground-state B3LYP density functional theory model and the LanL2DZ basis set were both used.[48] The optimization of the zinc oxide molecule is shown in Figure 6a−d, and this optimized molecule also interacted with the water molecule for the
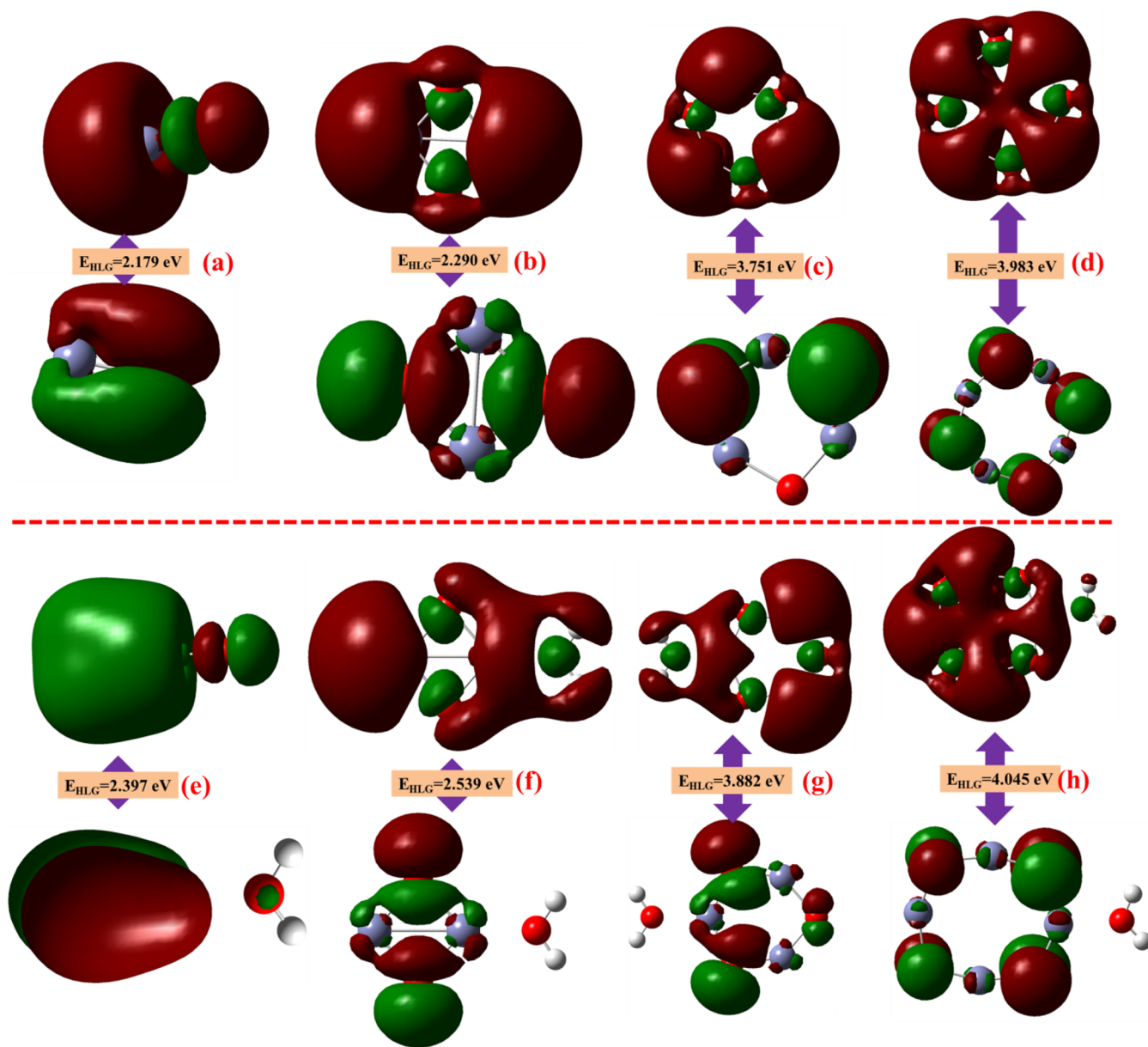
Figure 6. HOMO−LUMO gap representation of (a) 1ZnO, (b) 2ZnO, (c) 3ZnO, (d) 4ZnO, (e) 1ZnO-H_2O, (f) 2ZnO-H_2O, (g) 3ZnO-H_2O, and (h) 3ZnO-H_2O.

theoretical confirmation, which is also shown in Figure 6e−h. The energy level of the highest electron-containing molecular orbital is shown by the ZnO highest occupied molecular orbital (HOMO) energy levels, which vary from −6.629 to −6.835 eV. Simultaneously, the lowest unoccupied molecular orbital (LUMO) energy levels for ZnO range from −4.251 to −2.853 eV, signifying the energy level of the lowest unoccupied molecular orbital. The energy gap between the HOMO and LUMO levels in ZnO is known as the HOMO−LUMO gap energy, and it ranges from 2.179 to 3.983 eV. Additionally, upon interactions between ZnO and H_2O, particularly as it relates to the humidity sensing properties, the HOMO energy levels for ZnO-H_2O vary from −5.070 to −6.214 eV, revealing changes in electronic structure when in contact with water.[49] The influence of water on the electrical characteristics of the semiconductor is further shown by the LUMO energy levels for ZnO-H_2O, which span from −2.173 to −2.170 eV. Interestingly, ZnO-H_2O exhibits an HLG energy variation

ranging from 2.397 to 4.045 eV, suggesting variations in the energy needed for electron transitions when water is present.[50] From these observations, it can be clearly seen that upon interaction with water, the HLG energy of ZnO increases, which suggests lower conductivity, and this exactly resembles the experimental results.

For a more detailed study of the electronic properties, many other parameters calculated by relations S1−S10 are given in the Supporting Information, and the corresponding data with comparison study are presented in Figure S6a−d. The ionization potential and electron affinity values are calculated by using relations S2 and S3, respectively. The ionization potential values for ZnO vary from 5.995 to 6.856 eV, whereas the electron affinity values range from 2.853 to 4.251 eV. The energy needed to introduce and remove electrons from the system is reflected in these values, respectively. In contrast, the values of the ionization potential and electron affinity vary from 5.016 to 6.214 and 2.170 to 2.477 eV, respectively, when

ZnO interacts with water (ZnO-H₂O). The values for ZnO and its interaction with water ZnO-H₂O are included in Table S3 together with their electronegativity (relation S4) and chemical potential (relation S5). The electronegativity values for ZnO vary from 4.844 to 5.440 eV, indicating the atoms' propensity to draw electrons. For ZnO, the chemical potential values span from −4.844 to −5.440 eV, signifying the energy needed for the addition or removal of one electron. The electronegativity values of ZnO in water (ZnO-H₂O) exhibit a range of 3.621 to 4.981 eV, indicating alterations in the electron-attracting capacity brought about by the presence of water molecules. Chemical potential values of ZnO-H₂O vary from −3.621 to −4.981 eV, suggesting that the energy needed for electron-related reactions changes when water is present. Values for ZnO and its water interaction ZnO-H₂O for chemical hardness and chemical softness are shown in Table S3 and in relations S6 and S7, respectively. Chemical softness refers to how receptive a system is to changes in electron density, whereas chemical hardness measures how resistant a system is to such changes. The chemical hardness and chemical softness values for ZnO are 0.841 to 1.189 eV and 0.494 to 1.991 eV, respectively. Comparably, ZnO-H₂O has chemical softness and hardness ranges of 0.490 to 2.022 eV and 0.502 to 1.991 eV, respectively. These figures shed light on the stability and reactivity of ZnO and ZnO-H₂O, suggesting possible reactions to variations in electron density. Predicting the behavior of materials in a variety of chemical and electrical applications requires an understanding of chemical hardness and softness. A material's capacity to give electrons is indicated by its nucleophilic nature, which is reflected in the nucleophilicity index. The maximum charge transferred during a chemical process can be inferred from the charge transfer (Nmax). The charge transfer values for ZnO vary from 2.432 to 4.574 eV, whereas the nucleophilicity index (Nmax) spans from −12.443 to −5.891 eV. The nucleophilicity index (Nmax) and charge transfer values for ZnO-H₂O vary from −4.526 to −4.344 eV and from 2.073 to 2.951 eV, respectively.

Comparison of Theoretical and Experimental Data. Theoretical and experimental evidence plays complementary roles in increasing scientific understanding. Theoretical models inform experimental design, whereas experimental data develop and validate theoretical frameworks. To summarize, theoretical data are derived from models and predictions, whereas experimental data depend on direct observations and measurements. Both are important to the scientific method, and their combination enables a more comprehensive knowledge of natural events. In this work, according to the theoretical results, it has already been proven that the band gap of the material is increased 3.88 eV after interaction of humidity. This adsorption can change the zinc oxide electrical structure, causing band gap shifts, and the corresponding data are also shown in Table 1. Another explanation is that moisture can generate surface charges on zinc oxide. These surface charges can modify the energy levels of electrons within the material, hence affecting the band gap. The presence of water

on the surface can form dipoles or affect the surface potential, thus influencing the electrical structure. And this is the enhancement of the band gap at 3.91 eV. When zinc oxide with a suitable band gap encounters water vapor, its electrical conductivity changes. This is particularly true for semiconductors used in humidity sensors. As water molecules adsorb onto the material's surface, they can impact the transfer of charge carriers, causing differences in electrical conductivity. And the resistance is also enhanced, which is presented in our experimental studies.

■ CONCLUSIONS

The hydrothermal process was used to synthesize of ZNFs without any capping agent for humidity-sensing applications. The as-developed humidity sensor was employed to detect moisture in a regularly used device of the PPE Kit. From the experimental studies, we can observe that the ZNF material is a promising material for humidity sensors with short response and recovery times of 5.10 and 1.70 s in the humidity range of 10−95%RH. The highest sensitivity with good linearity in the humidity ranging from 50 to 95%RH was found as 296.70 nF/%RH with excellent repeatable performance at 45%RH. The simulation performed numerous studies on the computer model for the made zinc oxide. These findings established the groundwork for establishing the essential fact that the developed ZNF material is extremely appropriate for absorbent behavior and may be used for developing durable flexible devices for applications such as moisture monitoring. DFT studies in association with experimental data have exhibited its great potential in the field of metal oxides with exposure of analytes.

■ ASSOCIATED CONTENT

Ⓢ Supporting Information

The Supporting Information is available free of charge at https://pubs.acs.org/doi/10.1021/acs.langmuir.4c00366.

> Synthesis method; characterization techniques; SEM particle size; hysteresis of the sensor; statistical survey; sensitivity of the ZnO nanoflower (Table S1); comparison of other reported humidity sensors based on ZnO and composites (Table S2); DFT analysis; and electronic properties (Table S3) (PDF)

■ AUTHOR INFORMATION

Corresponding Authors

Meng-Fang Lin − *Department of Materials Engineering, Ming Chi University of Technology, New Taipei City 24301, Taiwan;* ⓞ orcid.org/0000-0002-9286-6527; Email: mflin@mail.mcut.edu.tw

Yu-Ching Huang − *Department of Materials Engineering, Ming Chi University of Technology, New Taipei City 24301, Taiwan;* ⓞ orcid.org/0000-0003-4772-8050; Email: huangyc@mail.mcut.edu.tw

B.C. Yadav − *Nanomaterials and Sensors Research Laboratory, Department of Physics, Babasaheb Bhimrao Ambedkar University, Lucknow, Uttar Pradesh 226025, India;* ⓞ orcid.org/0000-0001-7790-4647; Email: balchandra_yadav@rediffmail.com

Table 1. Theoretical and Experimental Band Gaps of the ZNFs

theoretical (band gap)		experimental (optical band gap)	
ZnO	ZnO-H₂O	ZnO	ZnO-H₂O
3.75 eV	3.88 eV	3.70 eV	3.91 eV

Authors

Priyanka Chaudhary − *Department of Materials Engineering, Ming Chi University of Technology, New Taipei City 24301, Taiwan;* ● orcid.org/0000-0003-4841-0888

Arpit Verma − *Nanomaterials and Sensors Research Laboratory, Department of Physics, Babasaheb Bhimrao Ambedkar University, Lucknow, Uttar Pradesh 226025, India;* ● orcid.org/0000-0001-7436-100X

Sandeep Chaudhary − *Department of Mathematics, Babasaheb Bhimrao Ambedkar University, Lucknow, Uttar Pradesh 226025, India*

Mahesh Kumar − *Department of Electrical Engineering, Indian Institute of Technology Jodhpur, Jodhpur 342011, India*

Kuen-Lin Chen − *Department of Physics, National Chung Hsing University, Taichung 40227, Taiwan*

Complete contact information is available at:
https://pubs.acs.org/10.1021/acs.langmuir.4c00366

Notes

The authors declare no competing financial interest.

■ REFERENCES

(1) Ates, H. C.; Nguyen, P. Q.; Gonzalez-Macia, L.; Morales-Narváez, E.; Güder, F.; Collins, J. J.; Dincer, C. End-to-end design of wearable sensors. *Nature Reviews Materials* **2022**, 7 (11), 887−907.

(2) Ates, H. C.; Yetisen, A. K.; Güder, F.; Dincer, C. Wearable devices for the detection of COVID-19. *Nature Electronics* **2021**, 4 (1), 13−14.

(3) Haick, H.; Tang, N. Artificial intelligence in medical sensors for clinical decisions. *ACS Nano* **2021**, 15 (3), 3557−3567.

(4) Aziz, A.; Pane, S.; Iacovacci, V.; Koukourakis, N.; Czarske, J. r.; Menciassi, A.; Medina-Sánchez, M.; Schmidt, O. G. Medical imaging of microrobots: Toward in vivo applications. *ACS Nano* **2020**, 14 (9), 10865−10893.

(5) Nasiri, S.; Khosravani, M. R. Progress and challenges in fabrication of wearable sensors for health monitoring. *Sensors and Actuators A: Physical* **2020**, 312, No. 112105.

(6) Gagnon, D.; Crandall, C. G. Sweating as a heat loss thermoeffector. *Handbook Clin. Neurol.* **2018**, 156, 211−232.

(7) Taylor, N. A.; Machado-Moreira, C. A. Regional variations in transepidermal water loss, eccrine sweat gland density, sweat secretion rates and electrolyte composition in resting and exercising humans. *Extreme Physiol. Med.* **2013**, 2 (1), 1−30.

(8) Wilke, K.; Martin, A.; Terstegen, L.; Biel, S. A short history of sweat gland biology. *International journal of cosmetic science* **2007**, 29 (3), 169−179.

(9) Fatima, Q.; Haidry, A. A.; Yao, Z.; He, Y.; Li, Z.; Sun, L.; Xie, L. The critical role of hydroxyl groups in water vapor sensing of graphene oxide. *Nanoscale Advances* **2019**, 1 (4), 1319−1330.

(10) Park, S.; Lee, D.; Kwak, B.; Lee, H.-S.; Lee, S.; Yoo, B. Synthesis of self-bridged ZnO nanowires and their humidity sensing properties. *Sens. Actuators, B* **2018**, 268, 293−298.

(11) Zhao, X.; Wang, P.; Li, B. J. CuO/ZnO core/shell heterostructure nanowire arrays: synthesis, optical property, and energy application. *Chem. Commun.* **2010**, 46 (36), 6768−6770.

(12) Zhang, Y.; Chung, J.; Lee, J.; Myoung, J.; Lim, S. J. Synthesis of ZnO nanospheres with uniform nanopores by a hydrothermal process. *J. Phys. Chem. Solids* **2011**, 72 (12), 1548−1553.

(13) Chen, L.; Zhang, J. J. Capacitive humidity sensors based on the dielectrophoretically manipulated ZnO nanorods. *Sens. Actuators, A* **2012**, 178, 88−93.

(14) Yu, S.; Zhang, H.; Chen, C.; Lin, C. J. Investigation of humidity sensor based on Au modified ZnO nanosheets via hydrothermal method and first principle. *Sens. Actuators, B* **2019**, 287, 526−534.

(15) Bacaksiz, E.; Parlak, M.; Tomakin, M.; Özçelik, A.; Karakız, M.; Altunbaş, M. The effects of zinc nitrate, zinc acetate and zinc chloride precursors on investigation of structural and optical properties of ZnO thin films. *J. Alloys Compd.* **2008**, 466 (1−2), 447−450.

(16) Singh, O.; Kohli, N.; Singh, R. C. Precursor controlled morphology of zinc oxide and its sensing behaviour. *Sens. Actuators, B* **2013**, 178, 149−154.

(17) Saidani, T.; Zaabat, M.; Aida, M.; Barille, R.; Rasheed, M.; Almohamed, Y. Influence of precursor source on sol−gel deposited ZnO thin films properties. *Journal of Materials Science: Materials in Electronics* **2017**, 28, 9252−9257.

(18) Alami, Z. Y.; Salem, M.; Gaidi, M. Effect of Zn concentration on structural and optical proprieties of ZnO thin films deposited by spray pyrolysis. *Adv. Energy Int. J.* **2015**, 2, 11−24.

(19) Lehraki, N.; Attaf, A.; Aida, M.; Attaf, N.; Othmane, M.; Bouaichi, F. Effect of different Zinc precursors in Structural and Optical properties of ZnO thin films. *arXiv preprint arXiv:2003.08487* **2020**, DOI: 10.48550/arXiv.2003.08487.

(20) Upadhyay, A.; Yang, H.; Zaman, B.; Zhang, L.; Wu, Y.; Wang, J.; Zhao, J.; Liao, C.; Han, Q. ZnO Nanoflower-Based NanoPCR as an Efficient Diagnostic Tool for Quick Diagnosis of Canine Vector-Borne Pathogens. *Pathogens* **2020**, 9 (2), 122.

(21) Verma, A.; Chaudhary, P.; Tripathi, R. K.; Yadav, B. Flexible, environmentally-acceptable and long-durable-energy-efficient novel WS 2−polyacrylamide MOFs for high-performance photodetectors. *Materials Advances* **2022**, 3 (9), 3994−4005.

(22) Chaudhary, P.; Maurya, D. K.; Pandey, A.; Verma, A.; Tripathi, R. K.; Kumar, S.; Yadav, B. Design and development of flexible humidity sensor for baby diaper alarm: Experimental and theoretical study. *Sens. Actuators, B* **2022**, 350, No. 130818.

(23) Gupta, M.; Chaudhary, P.; Singh, A.; Verma, A.; Yadav, D.; Yadav, B. Development of MoO3-CdO nanoparticles based sensing device for the detection of harmful acetone levels in our skin and body via nail paint remover. *Sens. Actuators, B* **2022**, 368, No. 132102.

(24) Zhang, Y.; Zhou, J.; Li, Z.; Feng, Q. Photodegradation pathway of rhodamine B with novel Au nanorods@ ZnO microspheres driven by visible light irradiation. *J. Mater. Sci.* **2018**, 53, 3149−3162.

(25) Huleihel, M.; Salman, A.; Erukhimovitch, V.; Ramesh, J.; Hammody, Z.; Mordechai, S. Novel spectral method for the study of viral carcinogenesis in vitro. *Journal of biochemical and biophysical methods* **2002**, 50 (2−3), 111−121.

(26) Muhammad, W.; Ullah, N.; Haroon, M.; Abbasi, B. H. Optical, morphological and biological analysis of zinc oxide nanoparticles (ZnO NPs) using Papaver somniferum L. *RSC Adv.* **2019**, 9 (51), 29541−29548.

(27) Jacob, R.; Isac, J. X-ray diffraction line profile analysis of Ba0. 6Sr0. 4FexTi (1-x) O3-δ,(x= 0.4). *Int. J. Chem. Stud* **2015**, 2, 12−21.

(28) Chang, F. M.; Brahma, S.; Huang, J. H.; Wu, Z. Z.; Lo, K. Y. Strong correlation between optical properties and mechanism in deficiency of normalized self-assembly ZnO nanorods. *Sci. Rep.* **2019**, 9 (1), 905.

(29) Guo, H.-L.; Zhu, Q.; Wu, X.-L.; Jiang, Y.-F.; Xie, X.; Xu, A.-W. Oxygen deficient ZnO 1− x nanosheets with high visible light photocatalytic activity. *Nanoscale* **2015**, 7 (16), 7216−7223.

(30) Qu, G.; Fan, G.; Zhou, M.; Rong, X.; Li, T.; Zhang, R.; Sun, J.; Chen, D. Graphene-modified ZnO nanostructures for low-temperature NO2 sensing. *ACS omega* **2019**, 4 (2), 4221−4232.

(31) Zhang, Q.; Zhao, X.; Duan, L.; Shen, H.; Liu, R. Controlling oxygen vacancies and enhanced visible light photocatalysis of CeO2/

ZnO nanocomposites. *J. Photochem. Photobiol., A* **2020**, *392*, No. 112156.

(32) Zhang, X.; Qin, J.; Xue, Y.; Yu, P.; Zhang, B.; Wang, L.; Liu, R. Effect of aspect ratio and surface defects on the photocatalytic activity of ZnO nanorods. *Sci. Rep.* **2014**, *4* (1), 1−8.

(33) Krishna, D. N. G.; Philip, J. Review on surface-characterization applications of X-ray photoelectron spectroscopy (XPS): Recent developments and challenges. *Applied Surface Science Advances* **2022**, *12*, No. 100332.

(34) Hu, Y.; Sun, L.; Liu, Z.; Liu, T. Controlled solvothermal synthesis of ZnO nanoparticles using non-destructive Mg-based channel templates for enhanced photocatalytic performance. *Mater. Chem. Phys.* **2023**, *299*, No. 127525.

(35) Ton-That, C.; Weston, L.; Phillips, M. Characteristics of point defects in the green luminescence from Zn-and O-rich ZnO. *Phys. Rev. B* **2012**, *86* (11), No. 115205.

(36) Gautam, C.; Verma, A.; Chaudhary, P.; Yadav, B. Development of 2D based ZnO−MoS2 nanocomposite for photodetector with light-induced current study. *Opt. Mater.* **2022**, *123*, No. 111860.

(37) Sharma, D. K.; Shukla, S.; Sharma, K. K.; Kumar, V. A review on ZnO: Fundamental properties and applications. *Materials Today: Proceedings* **2022**, *49*, 3028−3035.

(38) Duan, Z.; Jiang, Y.; Zhao, Q.; Wang, S.; Yuan, Z.; Zhang, Y.; Liu, B.; Tai, H. Facile and low-cost fabrication of a humidity sensor using naturally available sepiolite nanofibers. *Nanotechnology* **2020**, *31* (35), No. 355501.

(39) Zhao, J.; Li, N.; Yu, H.; Wei, Z.; Liao, M.; Chen, P.; Wang, S.; Shi, D.; Sun, Q.; Zhang, G. Highly sensitive MoS2 humidity sensors array for noncontact sensation. *Adv. Mater.* **2017**, *29* (34), No. 1702076.

(40) Mishra, S.; Lohia, P.; Chaudhary, P.; Yadav, B.; Dwivedi, D. Development of an impedance-based electrical humidity sensor using Sb-doped Ge-Se-Te chalcogenide glasses. *J. Electron. Mater.* **2020**, *49*, 6492−6500.

(41) Zhang, D.; Sun, Y. e.; Li, P.; Zhang, Y. Facile fabrication of MoS2-modified SnO2 hybrid nanocomposite for ultrasensitive humidity sensing. *ACS Appl. Mater. Interfaces* **2016**, *8* (22), 14142−14149.

(42) Bach, L. G.; Islam, M.; Hong, S.-S.; Lim, K. T. A simple preparation of a stable CdS-polyacrylamide nanocomposite: structure, thermal and optical properties. *J. Nanosci. Nanotechnol.* **2013**, *13* (11), 7707−7711.

(43) Ma, Z.; Fei, T.; Zhang, T. An overview: Sensors for low humidity detection. *Sens. Actuators, B* **2023**, *376*, No. 133039.

(44) Niu, H.; Yue, W.; Li, Y.; Yin, F.; Gao, S.; Zhang, C.; Kan, H.; Yao, Z.; Jiang, C.; Wang, C. Ultrafast-response/recovery capacitive humidity sensor based on arc-shaped hollow structure with nanocone arrays for human physiological signals monitoring. *Sens. Actuators, B* **2021**, *334*, No. 129637.

(45) Yadav, N.; Chaudhary, P.; Dey, K. K.; Yadav, S.; Yadav, B. C.; Yadav, R. R. Non-functionalized Au nanoparticles can act as high-performing humidity sensor. *Journal of Materials Science: Materials in Electronics* **2020**, *31*, 17843−17854.

(46) Yu, X.; Chen, X.; Ding, X.; Chen, X.; Yu, X.; Zhao, X. High-sensitivity and low-hysteresis humidity sensor based on hydrothermally reduced graphene oxide/nanodiamond. *Sens. Actuators, B* **2019**, *283*, 761−768.

(47) Frisch, A. J. W., USA, 25p, *gaussian 09W Reference*; Gaussian Inc. 2009, *470*.

(48) Vieira, W. T.; Bispo, M. D.; de Melo Farias, S.; de Almeida, A. d. S. V.; da Silva, T. L.; Vieira, M. G. A.; Soletti, J. I.; Balliano, T. L. Activated carbon from macauba endocarp (Acrocomia aculeate) for removal of atrazine: Experimental and theoretical investigation using descriptors based on DFT. *J. Environ. Chem. Eng.* **2021**, *9* (2), No. 105155.

(49) Kuik, M.; Wetzelaer, G. J. A. H.; Nicolai, H. T.; Craciun, N. I.; De Leeuw, D. M.; Blom, P. W. M. 25th anniversary article: charge transport and recombination in polymer light-emitting diodes. *Adv. Mater.* **2014**, *26* (4), 512−531.

(50) Haneef, H. F.; Zeidell, A. M.; Jurchescu, O. D. Charge carrier traps in organic semiconductors: a review on the underlying physics and impact on electronic devices. *Journal of Materials Chemistry C* **2020**, *8* (3), 759−787.